Nuclear Engineering and Technology 59 (2027) 104665

Contents lists available at ScienceDirect

Nuclear Engineering and Technology

journal homepage: www.elsevier.com/locate/net

Original Article

On unprotected loss-of-flow accident in a generic molten-salt reactor

Barbara Kędzierska [a,*], Philip Pfahl [b], Andrei Rineiski [a]

[a] Karlsruhe Institute of Technology, Institute for Neutron Physics and Reactor Technology, Hermann-von-Helmholtz-Platz 1, Eggenstein-Leopoldshafen, 76344, Germany
[b] Department of Ocean Operations and Civil Engineering, Norwegian University of Science and Technology, Larsgårdsvegen 2, Ålesund, 6009, Norway

ARTICLE INFO

Keywords:
Molten-salt reactor
Unprotected loss-of-flow (ULOF)
Delayed neutron precursors
Reactivity feedback
Transient analysis

ABSTRACT

Unprotected loss-of-flow (ULOF) transients in molten salt reactors (MSRs) are governed by a unique interplay between thermal-hydraulics and neutronics due to the circulation of the fuel salt, which carries the delayed neutron precursors (DNPs). This study analyzes a generic fast-spectrum molten chloride reactor, similar to the LOTUS design, during a ULOF accident using the SIMMER-III multi-physics code. The work investigates the previously observed double-peak in the power evolution and examines the conditions under which this behaviour occurs. The first power peak arises primarily from the retention of DNPs in the core as flow decreases, while the second peak is driven by the return of colder fuel salt from the heat exchanger, inserting positive reactivity. Between these peaks, a power valley occurs when negative temperature feedback temporarily dominates. A comprehensive parametric study examines the influence of key operational parameters on the magnitude, timing, and presence of these characteristic features. Results demonstrate that higher mass flow rates and longer coast-down times generally increase the amplitude of the first power peak, while lower heat exchanger temperatures and lower initial powers enhance both peaks and prolong oscillations. For high-power operation, and certain flow conditions, the double-peak behavior can be significantly damped or even eliminated. For MSRs operating at low power, the risk of significant power oscillations increases. For example, for the reference conditions, an initial power of 0.8 MW results in a first peak of approximately 104%, a subsequent valley of 55%, and a second peak of 108% of the initial power. Increasing the initial power to 3.2 MW under the same conditions eliminates the first peak, while the power decreases directly to 24% before recovering to 40% of the initial value. The analysis highlights the strong sensitivity of MSR transient behavior to steady-state design parameters and underscores the importance of accurately modelling DNP advection and heat exchanger performance in liquid-fuel reactor safety assessments.

1. Introduction

In most molten salt reactor (MSR) designs, the fuel is dissolved in a liquid salt circulating through the primary circuit [1]. This fundamental difference from solid-fuel reactors leads to a strong coupling between neutronics and thermal-hydraulics, particularly due to the movement of the delayed neutron precursors (DNPs) [2]. The flowing fuel affects the DNP distribution, leading to a lower effective delayed neutron fraction in the core and a different dynamic response compared to static-fuel reactors [3]. Accounting for the DNP drift and its impact on system transients is a challenge for numerical modelling, nevertheless is crucial for safety analysis [4]. An unprotected loss-of-flow (ULOF) accident is a transient in which the primary fuel-salt flow is lost or substantially reduced without an active reactor shutdown or other protective intervention. ULOF is an important scenario for liquid-fuel MSR because the reduction in the fuel circulation simultaneously affects the thermal hydraulics and the transport of the delayed neutron precursors, whose coupling can produce transient power excursions, making ULOF analysis important for evaluating the safety margins and dynamic behaviour of MSRs.

In a previous study of a thermal molten salt reactor, a ULOF transient was simulated [5]. The power evolution during that transient was characterized by two peaks before it finally decreased. The first peak was caused by retention of the DNPs due to the reduced flow rate, and the second peak resulted from the return of colder fuel from the heat exchanger. These two mechanisms are unique to liquid-fuel reactors, and the resulting peaks are not observed in ULOF transients of other reactor types [6].

Understanding and correctly predicting these coupled feedback mechanisms is important for establishing normal operating parameters

* Corresponding author.
E-mail address: barbara.kedzierska@kit.edu (B. Kędzierska).

https://doi.org/10.1016/j.net.2026.104665
Received 6 May 2026; Received in revised form 12 August 2026; Accepted 17 August 2026
Available online 21 August 2026

in MSR. This is particularly important during the reactor startup where power and thermal feedback are generally lower. In these conditions, a change in fuel flow might lead to large power augmentation caused by cold fuel and DNPs reentering into the core [7,8]. While prior work has demonstrated this double-peak behaviour in thermal MSRs, its occurrence and dependence on reactor configuration have not been systematically characterised. To investigate whether the same underlying mechanisms can also occur in other MSR configurations, we study a different MSR model compared to the thermal graphite moderated reactor in Ref. [5], namely a fast-spectrum molten chloride reactor similar to the LOTUS reactor [9]. The distinct neutron physics of different MSR systems, including DNP fractions, spectra, and temperature feedback coefficients, makes this comparison non-trivial and provides stronger evidence that the mechanisms leading to a double-peak behaviour are not restricted to the previously studied thermal MSR configuration.

The central novel contribution of this paper is a comprehensive parametric study of the ULOF transient response, investigating the effect that the mass flow rate (*MFR*), power, heat exchanger temperature T_{HX}, and the coast-down time *CDT* have on the power evolution and the presence of those peaks. Optimizing these parameters can lead to more predictable reactor behaviour during ramping and accident scenarios, and may inform operational safety margins relevant to MSR licensing and design. This is particularly timely given growing industrial interest in fast-spectrum chloride reactors and the need for validated transient analysis tools to support their deployment [10].

In this paper, the software SIMMER-III is used, a severe accident code developed by the Japan Atomic Energy Agency in cooperation with international partners, including the Karlsruhe Institute of Technology [11]. It couples a thermal hydraulic module with a time- and space-dependent neutron transport solver and a structure module. SIMMER-III is selected here because it has been validated for MSR applications [12,13] and its coupled neutronics-thermal hydraulics framework is well suited to capturing the DNP drift dynamics central to this study. The presented model assumes a plug flow and does not account for turbulence and other flow patterns that might affect the observed transients.

In section 2, we first introduce the used reactor model, the simulated domain, the salt properties, and the operational parameters. The model is a simplified reactor system similar to LOTUS [9].

In section 3, we describe a ULOF transient and present the reactor response in terms of power and reactivity. Important phases and points during the transient are described, and the underlying mechanisms are explained.

In section 4, the heat exchanger temperature, the coast down time, the initial power, and the mass flow rate are changed. Their effect on the ULOF transient is discussed, and the power and reactivity evolutions are presented. Then the ULOF is repeated for fixed power to mass flow rate ratios, since this ratio defines the temperature rise in the core.

In section 5, the full parametric study is presented, allowing for a systematic interpretation of the results. A few particular transients are shown and discussed.

In section 6, the results of the paper are summarized.

2. Simulation

2.1. MSR model

The fast MSR model consists of a cylindrical core surrounded by a layer of magnesium oxide reflector. The design is similar to the LOTUS and MCRE designs ([9,14]). The computational domain is two-dimensional, axisymmetric, with a core and a reflector region. The primary loop is represented by the core and an out-of-core section containing the heat exchanger. Fuel salt enters the lower part of the core, flows upward through the core, and is heated up by the fission power. At the core outlet, the fuel enters the out-of-core section, where it is cooled in the heat exchanger before returning to the core inlet. Delayed neutron precursors are transported together with the flowing fuel salt and therefore circulate between the core and the out-of-core region.

Fig. 1 shows a scheme of the reactor core in the middle, a reflector colored in grey and the heat exchanger colored in green. The considered model has a cylindrical reactor core with a height of $H = 1.287$ m and a diameter $D = 0.515$ m. The reflector width is $w = 0.55$ m on both sides. In this simplified model, the heat transfer between the salt and the reflector is not considered. The reflector is at a constant temperature of 900 K.

The model includes an out-of-core section to simulate the fuel outside the core. The fuel is flowing upwards through the reactor core, enters the heat exchanger area and returns into the core from the bottom. With the fuel the DNPs are advected with the fuel flow upwards, out of the core and reenter at the reactor bottom. The fuel returns at a temperature of $T_{inlet} = 900$ K and is heated by the fissions in the core. The temperature rise through the core is 12.5 K. The residence time of the fuel in the core is 8.71 s and the circulation time is 10.456 s with a fuel bulk velocity of $v = \sim 0.1477$ m/s, the mass flow rate $MFR = 100$ kg/s, the power $P_0 = 0.8$ MW, and the heat exchanger temperature $T_{HX} = 850$ K. The out-of-core region is one dimensional. At the reactor inlet boundary the fuel is adjusted according to the outlet parameters and the transient time. With slightly less than 20% of the fuel salt outside the core, the system is characterised by relatively short out-of-core times. The initial power of 0.8 MW is used as the reference operating condition of the simplified generic reactor model. This reference value is selected to provide a baseline for investigating the coupled DNP and thermal feedback mechanisms and can be relevant for research facilities and for the reactor start-ups. The key model parameters are given in Table 1.

In the heat exchanger the fuel is cooled. The resulting change in the inlet temperature

$$T_{inlet}(t) = T_{HX} + (T_{outlet}(t - t_{ooc}(t)) - T_{HX}) \cdot e^{-\gamma t_{ooc}(t)} \quad \text{(Eq. 1)}$$

with the time t,the out-of-core (ooc) residence time t_{ooc} of a particle returning to the core at time t, the heat exchanger second side temperature T_{HX}, the temperature at the outlet T_{outlet}, and the heat exchanger heat transfer efficiency parameter γ. To calculate the out-of-core residence time we use the model developed by R. C. Diniz et al. [15].

The out-of-core configuration is an important aspect of the analysed transient. In particular, the reactor designs with substantially different primary loop layouts or heat exchanger characteristics may exhibit stronger or weaker effects on the investigated features. The selected

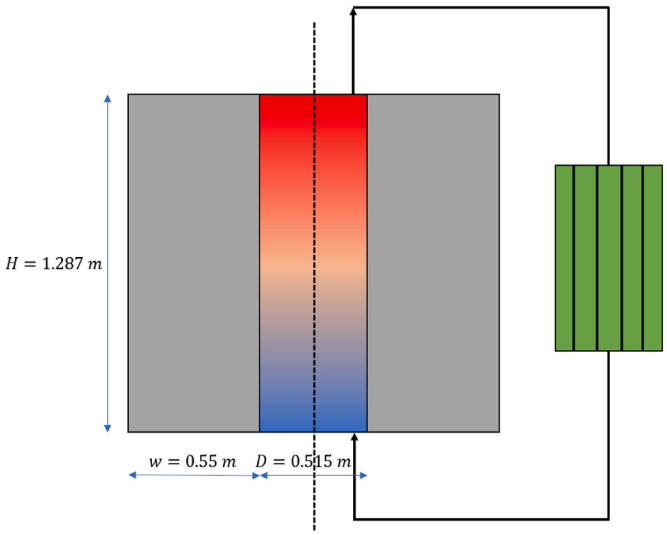

Fig. 1. Scheme and dimensions of the MSR model.

Table 1
Key model parameters.

Parameter	Value
Core height	1.287 m
Core diameter	0.515 m
Reflector width	0.55 m
Core salt volume	0.268 m^3
Out-of-core salt volume	0.063 m^3
Total salt volume	0.331 m^3
Nominal mass flow rate	100 kg/s
Nominal fuel velocity	0.1477 m/s
Nominal power	0.8 MW
Heat exchanger temperature	850 K
Core temperature rise	12.5 K
Reflector temperature	900 K
Delayed neutron fraction β	661 pcm
Effective delayed neutron fraction β_{eff}	742 pcm
Prompt neutron generation time	$7.35657{\cdot}10^{-6}$ s
Fuel salt composition	$^2/_3$ NaCl + $^1/_3$ UCl_3
Uranium enrichment	93.2%wt

model is therefore intended to investigate the coupled DNP drift and cold-salt-return mechanisms for the generic loop configuration, rather than to represent all possible liquid-fuel MSR configurations.

The fuel salt is $^2/_3$ NaCl + $^1/_3$ UCl_3 with uranium enriched to 93.2% wt. All the other elements, including chlorine, are used in natural composition. Natural chlorine is retained in the present model because a large-scale enrichment of chlorine isotopes has not been demonstrated at an industrial scale yet [16], and is motivated by TerraPower choice [17]. The neutron absorption associated with ^{35}Cl is included in the neutronics calculations. The temperature-dependent thermophysical properties of the fuel salt are based on the correlations reported in Ref. [14] and are presented in Table 2. The corresponding feedback coefficients are provided in Table 3, obtained with SIMMER for the reactor model and fuel composition described above. The constants have been calculated for the range 800 – 950 K.

In the analysed reactor, the delayed neutron fraction $\beta = 661$ pcm. In the present simulations, six delayed neutron precursor groups are used, each of them is characterised by its own delayed neutron fraction and precursor decay constant, as shown in Table 4. The effective beta fraction $\beta_{eff} = 742$ pcm. The delayed neutron fraction due to the fuel flow and DNP advection β_{flow} is 578 pcm. The adjoint-weighted prompt neutron generation time calculated by SIMMER is $7.35657{\cdot}10^{-6}$ s.

2.2. SIMMER software

SIMMER-III is a severe accident code, extended for MSR applications. It consists of a two-dimensional, mutli-component, multi-field, Eulerian model for thermohydraulic calculations coupled to a space-dependent kinetics neutronic transport model.

In MSR the DNPs are advected with the fuel flow. In SIMMER, the current DNP concentration for each group is calculated from the stationary DNP concentration $C_s(r,t)$ and a modification term $C_m(r,t)$

Table 3
Reactivity feedback coefficients obtained with SIMMER.

Feedback	Value
Fuel temperature [pcm/K]	−11.99
Fuel Doppler [pcm/K]	−0.03
Fuel density [pcm/(kg/m^3)]	−11.28
Reflector [pcm/K]	−0.013

$$C(r,t) = C_s(r,t) + C_m(r,t). \quad \text{(Eq. 2)}$$

$C_m(r,t)$ is calculated in the Eulerian model.

The "movable term" is then integrated with the weight of the adjoint flux in the core region:

$$c_m \sim \int_V w(r)\, C_m(r,t)\, dV. \quad \text{(Eq. 3)}$$

The change in the reactivity balance equation (or point-kinetics equation) caused by the advection of the DNPs is calculated by evaluating the delayed source term at each quasi-static time step. This change can be expressed by ρ_{loss}, a difference between the effective delayed neutron fraction β_{eff} and the one in the system with the flowing source β_{flow}:

$$\rho(t)_{loss} = -\frac{c_m(t)\,\Lambda}{A(t)\,\beta_{eff}}, \quad \text{(Eq. 4)}$$

where Λ (t) is the prompt neutron generation time, $A(t)$ is the neutron flux amplitude, and β_{eff} is the effective delayed neutron fraction.

At steady state, ρ_{loss} is compensated by a positive reactivity, $\rho_{compensate} = \rho(t=0)_{loss}$. With those terms the total DNP effect is

$$\rho_{DNP}(t) = \rho(t)_{loss} + \rho_{compensate} \quad \text{(Eq.5)}$$

Given the definition of reactivity:

$$\rho_{temp}(t) = \frac{k_{eff}(t) - 1}{k_{eff}(t)} = 1 - \frac{1}{k_{eff}(t)}, \quad \text{(Eq.6)}$$

the reactivity change caused by changes in the temperature is obtained from the reciprocal difference in the eigenvalue between the current state and the reference state (steady state) at time t = 0, so that

$$\rho_{temp}(t_1) = \frac{1}{k_{eff}(t_0)} - \frac{1}{k_{eff}(t_1)}. \quad \text{(Eq.7)}$$

The total reactivity is the sum of the temperature/density reactivity effect and the delayed neutron effect:

$$\rho_{total} = \rho_{temp} + \rho_{DNP}. \quad \text{(Eq. 8)}$$

The reactivity is reported in dollars in the following, where one dollar is equal to the steady-state delayed neutron source.

Table 2
Temperature-dependent salt properties, based on [14].

Property	Formula
Melting temperature	$523\ ^\circ C = 796.15\ K$
Density	$\rho\left[\frac{kg}{m^3}\right] = 4.2126{\cdot}10^3 - 1.0686{\cdot}T[K]$
Specific heat capacity	$c_p\left[\frac{J}{kg{\cdot}K}\right] = 8.900439{\cdot}10^3 - 13.77936{\cdot}T[K] + 6.400369{\cdot}10^{-3}{\cdot}T[K]^2 - \frac{8.443758{\cdot}10^8}{T[K]^2}$
Thermal conductivity	$\lambda\left[\frac{W}{m{\cdot}K}\right] = 5.6820 - 8.7832{\cdot}10^{-3}{\cdot}T[K] + 4.0967{\cdot}10^{-6}{\cdot}T[K]^2 - \frac{5.7642{\cdot}10^5}{T[K]^2}$
Dynamic viscosity	$\mu\,[Pa{\cdot}s] = 1.505{\cdot}10^{-4}{\cdot}exp\left(\frac{2.666{\cdot}10^4}{8.314{\cdot}T[K]}\right)$

Table 4
Delayed neutron fractions and decay constants for six groups.

Group number	1	2	3	4	5	6
β	0.000232454	0.00122393	0.00120464	0.00332969	0.000998859	0.000346472
λ [s^{-1}]	0.0124905	0.0318108	0.109413	0.317187	1.35335	8.65788

3. Unprotected loss of flow transient description

An unprotected loss of flow is an accident scenario in a nuclear reactor in which the primary coolant pump stops, causing the flow rate reduction until a new steady state is reached. During the transient, no active measures are taken to mitigate the accident and the reactor parameters evolve freely without any external interaction.

Generally, a ULOF is modelled by reducing the pumping power in a steady-state reactor. Since the used model lacks an explicitly modelled pump, a ULOF is represented by a prescribed reduction in the salt velocity, which serves as the flow boundary condition. The inlet velocity is therefore linearly reduced from 100% at the start of the transient to 10%. The time required for this reduction is called the Coast-Down Time (*CDT*).

In Fig. 2, the power and reactivity evolution during the first 200 s of a ULOF transient are shown for the initial mass flow rate $MFR = 100$ kg/s, the initial power $P_0 = 0.8$ MW, and the heat exchanger temperature $T_{HX} = 850$ K, with a *CDT* of 10 s. The power is given as a ratio to the initial power P/P_0 on the left axis, while the reactivity is shown on the right axis in dollars ($). The reactivity is split into its temperature and DNP component.

The power curve in Fig. 2 is characterized by two peaks: ***peak 1***, which appears at the beginning of the transient, and ***peak 2***, which follows after a drop in power called ***valley 1***. In the curve, a few characteristic regions can be distinguished:

- Region **I** from time t = 0 to ***peak 1***:

Shortly after the inlet velocity goes down, two competing phenomena come into play. The decreased velocity at the outlet retains more DNPs in the core, which would otherwise leave the core and emit neutrons in the out-of-core region. These additional neutrons emitted in the core contribute to more fission and increase in the reactivity. At the same time, fluid remaining in the core for a longer time absorbs more fission power and its temperature starts to increase. These competing phenomena determine the magnitude of ***peak 1***. In some cases, the magnitude of this peak might be zero.

- Region **II** from ***peak 1*** to ***valley 1***:

The decrease of power toward the valley occurs when the negative feedback from the heated salt starts to dominate over the DNP retention feedback. The power continues to decrease until colder fluid from the heat exchanger starts to enter the core.

- Region **III** from ***valley 1*** to ***peak 2***:

The cooler liquid brings positive reactivity to the core. The fluid which has spent a longer time in the heat exchanger reaches the core inlet and travels through the core, resulting in an increase in reactor power. Eventually, the reactor power is high enough to heat up the fluid to the temperature at which the reactivity balances the instantaneous DNP feedback.

- Region **IV** from ***peak 2*** to ***valley 2***:

The temperature feedback in the core reaches the point at which the reactivity starts to drop. The incoming salt temperature increases and, together with the hot salt in the core, causes the power to decline again.

- Region **V** after ***valley 2***:

The curve oscillates until the new steady state is reached. Reaching the new steady state in such a short time is only possible because the temperature feedback from the structures is neglected in this model. It takes several oscillations, resulting from the change in the outlet temperature, affecting the inlet temperature, as well as from the cyclic inflow of periodically changing amount of DNPs, produced proportionally to the reactor power, before the system stabilizes.

4. Effect of single parameter change

In order to understand the ULOF transient better, a parametric study has been carried out. An objective of the study is to show how different reactor parameters influence the shape of the transient. Several pa-

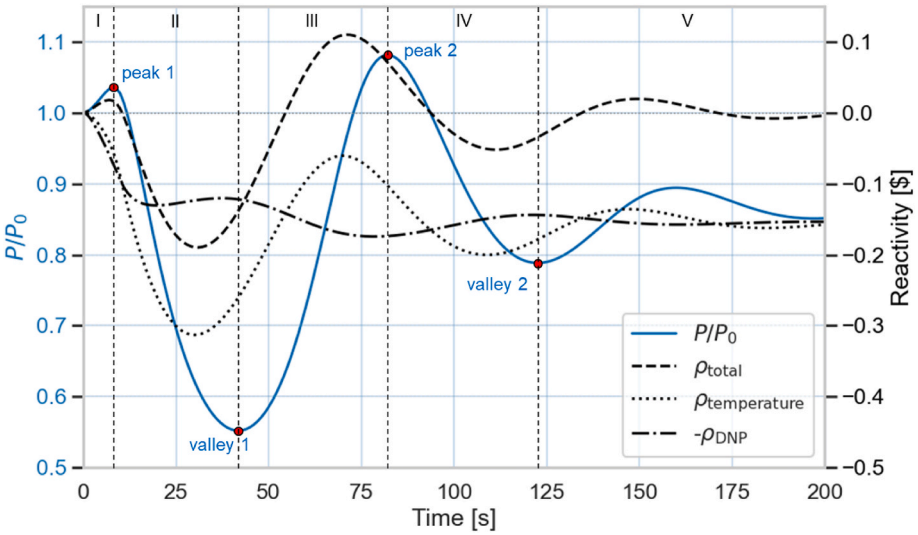

Fig. 2. Power and reactivity contribution from the fuel temperature and DNP advection.

Table 5
Range of parameters changed for the transients.

T_{HX} [K]	800 - 890
CDT [s]	1 - 50
P_0 [MW]	0.8 - 3.2
MFR [kg/s]	25 - 400
P_0 / *MFR* [W·s/kg]	8000 - 32000

rameters are investigated to identify which of them make peaks more or less pronounced, and how the timing of the peaks changes. In this section, the heat exchanger temperature, the coast down time, the initial power, the mass flow rate, and the power-to-mass-flow ratio are changed individually. The range of parameters is shown in Table 5. The heating parameter γ is adjusted in order to keep the inlet temperature constant at $T_{inlet} = 900$ K for steady states at different steady state power levels, inlet heat exchanger temperatures, and velocities. While each parameter change is discussed individually, all the other parameters are kept as in the model described in Section 2. The results corresponding to the original model are always shown in red.

4.1. Effect of different heat exchanger temperatures

For ULOF transients, the heat exchanger temperature plays a vital role, since the residence time in the heat exchanger changes. Here, the initial power $P_0 = 0.8$ MW, initial mass flow rate $MFR = 100$ kg/s, and $CDT = 10$ s are kept constant, while the heat exchanger temperature is changed. The values are summarized in Table 6.

In Fig. 3, the ULOF transient is shown for the different heat exchanger temperatures, and in Fig. 4, the reactivity with its components for two selected cases is presented.

For the highest heat exchanger temperature $T_{HX} = 890$ K, ***peak 1*** has the lowest magnitude. In all the presented cases, the reduction in the mass flow rate induces a positive reactivity insertion of the DNPs returning into the core. The immediate positive DNP feedback due to their retention in the core is approximately the same for these three cases, while the temperature feedback is different. The heating of the fuel causes a negative reactivity insertion. For a heat exchanger temperature of $T_{HX} = 890$ K the sum of these reactivity feedbacks is the smallest. The difference is caused by the fact that the immediate positive DNP feedback due to their retention in the core is approximately the same for these three cases, while the negative insertion is largest for $T_{HX} = 890$ K.

As the heating parameter γ (Eq. (1)) is adjusted to keep the T_{inlet} the same at all the steady states, when the cooling time increases in the same way for all the three cases, the inlet temperature decreases faster for lower T_{HX}. The inflow of the cold salt makes ***peak 1*** more pronounced at lower heat exchanger temperatures. Additionally, ***peak 1*** is observed earlier at higher temperatures, and is later damped by the negative temperature feedback. The difference in timing of this peak is mainly driven by the difference in the temperature response - in Fig. 4 the temperature feedback curves diverge earlier than the DNP feedback curves.

Valley 1 is deeper and occurs later for higher heat exchanger temperatures. It is driven by the increase of the in-core salt temperature. Then, power increases again and reaches ***peak 2***, which might be higher than the initial power P_0 for lower heat exchanger temperatures, at which it also appears earlier. In contrast, at the highest heat exchanger temperature, ***peak 2*** has a relatively small magnitude and occurs later, and a new steady state is reached faster than at lower T_{HX}.

Table 6
Parameters used to study the effect of the heat exchanger temperature T_{HX}.

MFR [kg/s]	P_0 [MW]	T_{HX} [K]	*CDT* [s]
100	0.8	800, 850, 890	10

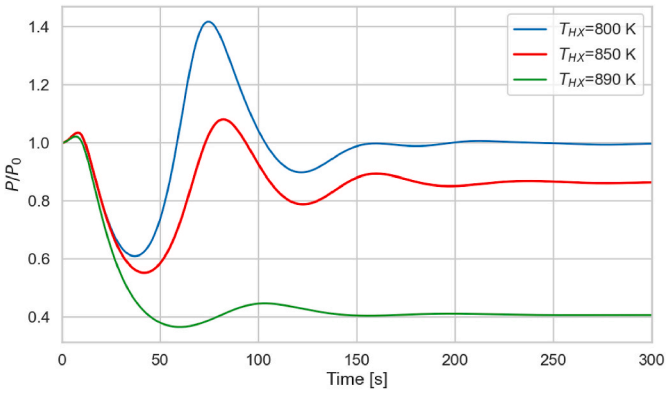

Fig. 3. Power change during the ULOF transient for different T_{HX} with $MFR = 100$ kg/s, $P_0 = 0.8$ MW, $CDT = 10$ s.

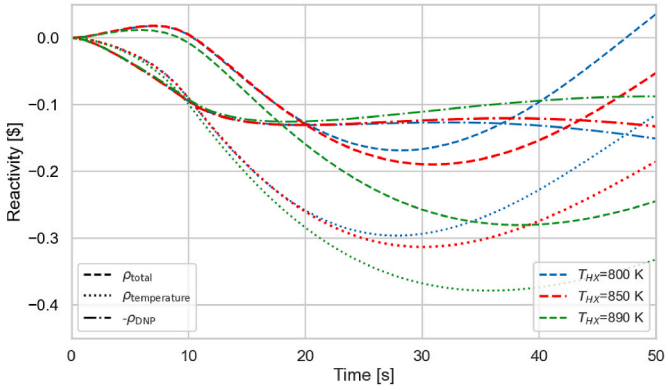

Fig. 4. Reactivity change during the ULOF transient for different T_{HX} with $MFR = 100$ kg/s, $P_0 = 0.8$ MW, $CDT = 10$ s.

In conclusion, a lower heat exchanger temperature is less efficient at damping the power transient. It results in a shallower ***valley 1*** and a more pronounced ***peak 2***. As expected, a lower heat exchanger temperature leads to a lower inlet temperature at the new steady state, which is found at a higher power level than for higher heat exchanger temperatures.

4.2. Effect of different CDT

The *CDT* dictates the slope at which the pump stops. The initial mass flow rate $MFR = 100$ kg/s, power $P_0 = 0.8$ MW, and the heat exchanger temperature $T_{HX} = 850$ K are kept constant. The *CDT* changes from 1 to 50 s. The values are summarized in Table 7.

In Fig. 5, the ULOF transient is shown for different *CDT*s, and, in Fig. 6, the reactivity and its components are plotted for the selected *CDT* values.

For a larger *CDT*, ***peak 1*** occurs later and is higher than for smaller *CDT*s. In the selected cases, during the initial phase of the transient, the total reactivity feedback is positive for all *CDT*s, but the difference between the temperature and DNP contributions is significantly larger for large *CDT*s. For a larger *CDT*, the fuel velocity reduces slower. Therefore, the amount of the DNPs retained in the core increases slowly. Their slowly increasing amount results in a slow increase in the positive

Table 7
Parameters used to study the effect of *CDT*.

MFR [kg/s]	P_0 [MW]	T_{HX} [K]	*CDT* [s]
100	0.8	850	1, 5, 10, 15, 20, 30, 50

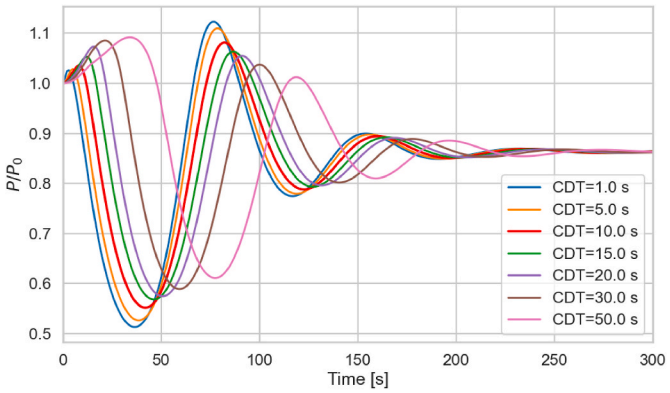

Fig. 5. Power change during the ULOF transient for different *CDT*s with $MFR = 100$ kg/s, $P_0 = 0.8$ MW and $T_{HX} = 850$ K.

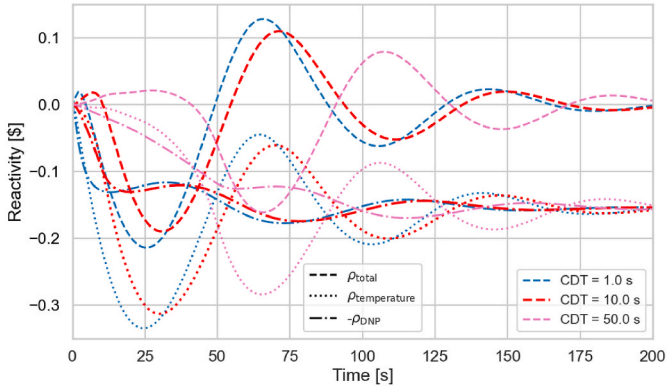

Fig. 6. Reactivity change during the ULOF transient for different *CDT* s with $MFR = 100$ kg/s, $P_0 = 0.8$ MW, $T_{HX} = 850$ K.

reactivity insertion due to the DNP movement. The slower velocity decrease changes the fuel temperature slower compared to smaller *CDT*s; therefore the temperature reactivity feedback also increases slower. The combined effect of these two reactivity contributions can be observed for two *CDT* cases in Fig. 6. From the beginning of the transient, in both cases the DNP reactivity curve decreases faster than the temperature reactivity curve, but the difference is larger for a large *CDT*. When the curves cross, the total reactivity changes its sign to become negative, and the power shortly starts to decrease.

For smaller *CDT*s, the DNPs are more strongly retained in the core and the temperature rises more quickly.

For a larger *CDT*, ***valley 1*** is shallower, as a consequence of the slower-acting and less effective temperature feedback. After ***valley 1***, the power curve increases to ***peak 2***, which is lower for the larger *CDT*s. At a larger *CDT*, the amplitudes of the negative temperature reactivity feedback are smaller, therefore the power oscillation amplitudes are also smaller.

Table 8
Parameters used to study the effect of P_0.

MFR [kg/s]	P_0 [MW]	T_{HX} [K]	*CDT* [s]
100	0.8, 1.6, 2.4, 3.2	850	10

4.3. Effect of different initial power

In Fig. 7, the ULOF transient is compared for different initial power of $P_0 = 0.8$ MW, 1.6 MW, 2.4 MW, and 3.2 MW (see Table 8), with the initial mass flow rate $MFR = 100$ kg/s, heat exchanger temperature $T_{HX} = 850$ K, and pump coast-down time $CDT = 10$ s. The associated reactivity changes are shown in Fig. 8. At steady state, these systems are characterized by a different temperature rise in the core and by the same loss of reactivity due to the DNP advection. This range is used to assess whether the transient mechanisms identified for the 0.8 MW reference case persist when the reactor operating power is increased.

In Fig. 7, ***peak 1*** is only visible for the lowest initial power $P_0 = 0.8$ MW. At higher power, the power curve decreases immediately, with the steepest slope for the highest initial power $P_0 = 3.2$ MW. This behaviour can be explained by different relative contributions of the reactivity feedback components compared to previous subsections. At lower power, during the first seconds of the transient, the positive change in the DNP feedback is larger than the negative change in the temperature feedback, resulting in a temporary power increase. However, at higher initial power, the negative temperature feedback in the first seconds of the transient is much stronger than the positive DNP feedback. Thus, at higher power, the positive change in the DNP feedback is much smaller, while the negative change in the temperature feedback is significantly larger. This causes an immediate power decrease without presence of ***peak 1***.

For the initial power $P_0 = 3.2$ MW, ***valley 1*** is the deepest, because the temperature changes the most in the core. The system, initially operating with a large core temperature rise, experiences more negative reactivity insertion when the velocity decreases and the fuel heats up. For lower initial power, ***peak 2*** is higher than for higher initial powers, which is caused by stronger temperature feedback. The magnitude of the temperature feedbacks for initial power $P_0 = 0.8$ MW and 3.2 MW can be compared in Fig. 8. At lower power, ***peak 2*** occurs slightly later than at higher power, which is caused by a faster damping of the power oscillations.

The inlet and outlet temperature are shown in Fig. 9. For higher

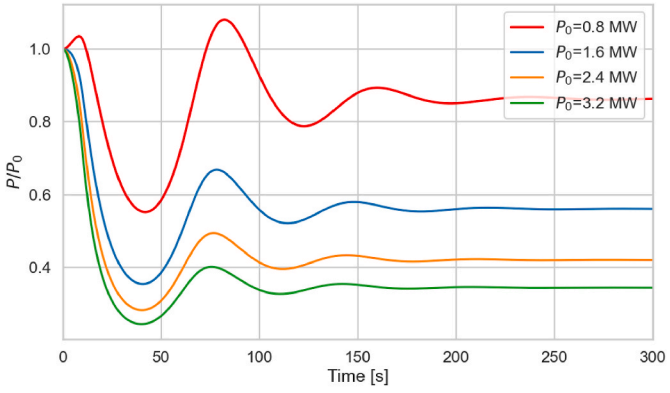

Fig. 7. Power change during the ULOF transient for different P_0 with $MFR = 100$ kg/s, $T_{HX} = 850$ K, $CDT = 10$ s.

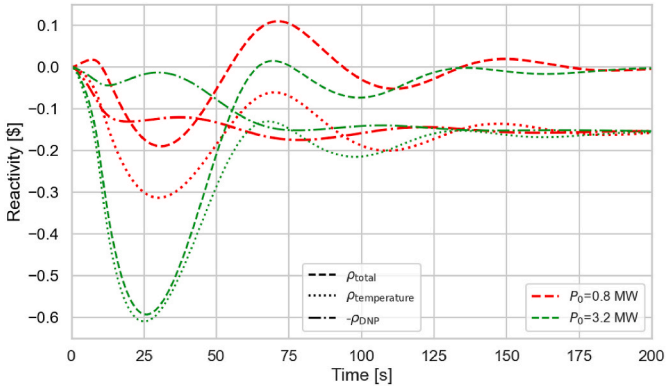

Fig. 8. Reactivity change during the ULOF transient for different P_0 with $MFR = 100$ kg/s, $T_{HX} = 850$ K, $CDT = 10$ s.

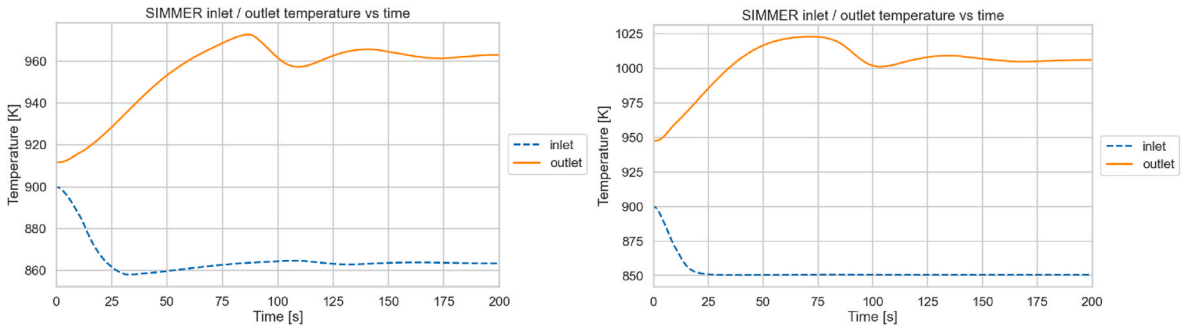

Fig. 9. Temperature change during the ULOF transient for $P_0 = 0.8$ MW (left) and 3.2 MW (right), with $MFR = 100$ kg/s, $T_{HX} = 850$ K, $CDT = 10$ s.

power, the inlet temperature quickly converges to that close to the heat exchanger temperature, while at lower power several temperature oscillations occur before the new inlet temperature is reached. These oscillations in the inlet temperature result in longer-lasting oscillations in power.

4.4. Effect of different mass flow rates

The mass flow rate of the model was varied from $MFR = 25$ to 100 kg/s, while keeping the initial power at $P_0 = 0.8$ MW, the heat exchanger temperature $T_{HX} = 850$ K, and the pump coast-down time $CDT = 10$ s. The used parameters are summarized in Table 9. In Table 10, the corresponding out-of-core times, inlet velocities, and the ρ_{loss} are shown for different MFRs.

In Fig. 10, the ULOF transient is shown for the different mass flow rates at a fixed power $P_0 = 0.8$ MW, heat exchanger temperature $T_{HX} = 850$ K, and transient time $CDT = 10$ s. The reactivity and its components for two selected mass flow rates ($MFR = 25$ and 100 kg/s) are shown in Fig. 11.

At steady state, in a system characterised by a higher mass flow rate, more DNPs are flushed out of the core and they emit neutrons in the out-of-core region of smaller importance to the total fission source. In this case, the difference between the static β_{eff} and flowing β_{flow} is larger. Therefore, when a loss-of-flow transient starts, the same drop in the velocity expressed in per cent, at higher initial mass flow rates corresponds to a larger change between β_{eff} and β_{flow}. This effect is larger than the negative insertion from the temperature feedback.

At higher initial mass flow rate, the power initially increases from the initial power $P_0 = 0.8$ MW and reaches ***peak 1***, as observed for the initial mass flow rates of $MFR = 100$ kg/s and $MFR = 75$ kg/s. In case of a lower initial mass flow rate, the initial reactivity insertion from the DNP retention is lower, and, more importantly, the positive DNP reactivity feedback is weaker than the negative feedback due to salt temperature increase. From the beginning of the transient, the net effect is negative, and the total reactivity feedback monotonically decreases, preventing the ***peak 1*** to appear.

This combination at the lower mass flow rate results in a smoother but slower decrease of power to ***valley 1***, which is deeper than for higher mass flow rates. ***Valley 1*** is followed by a low ***peak 2***, caused by the decrease of the average temperature in the core. At the highest initial mass flow rate $MFR = 100$ kg/s, ***peak 2*** is exceeds the initial power P_0. At low mass flow rate, the changes in the temperature feedback have larger amplitude than at higher mass flow rates. In contrast, the changes of β_{eff} at lower mass flow rate have smaller amplitudes than at higher mass flow rates, and a smaller change in β_{eff} happens to the new steady state.

Table 9
Parameters used to study the effect of *MFR*.

MFR [kg/s]	P_0 [MW]	T_{HX} [K]	*CDT* [s]
25, 50, 75, 100	0.8	850	10

Table 10
Comparison of steady-state model parameters for different *MFR* s.

Mass flow rate [kg/s]	Out-of-core time [s]	Inlet velocity [m/s]	ρ_{loss} [pcm]
25	8.19	0.03693	88
50	4.095	0.07386	127
75	2.73	0.11078	150
100	2.0475	0.14771	165

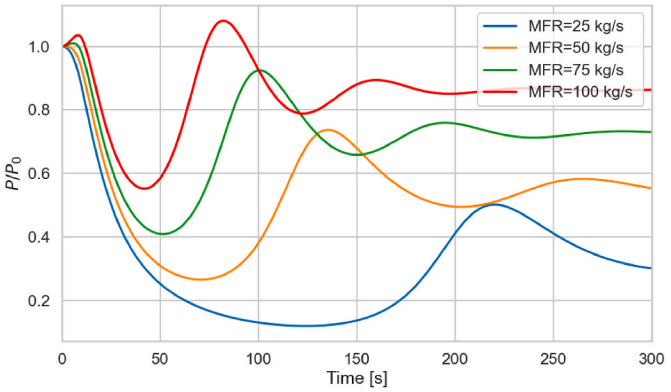

Fig. 10. Power change during the ULOF transient for different *MFR* with $P_0 = 0.8$ MW, $T_{HX} = 850$ K, $CDT = 10$ s.

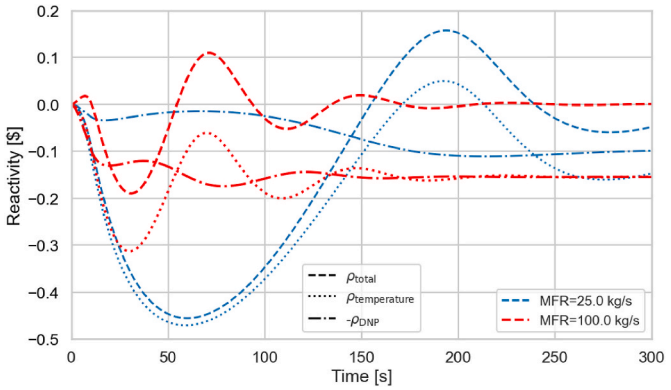

Fig. 11. Reactivity change during the ULOF transient for different *MFR* with $P_0 = 0.8$ MW, $T_{HX} = 850$ K, $CDT = 10$ s.

While for the system with an initial mass flow rate $MFR = 100$ kg/s, the DNP feedback stabilizes after approximately 200 s into a transient, the temperature reactivity feedback oscillations are still visible by slow convergence to a new steady-state power level.

In conclusion, the difference in mass flow rate is visible by different

steady-state reactivity corresponding to the DNPs and temperature. During a transient, a higher initial mass flow rate results in a higher ***peak 1***, shallower ***valley 1*** and more pronounced ***peak 2***. All these characteristic points and a new steady state are reached earlier for a higher initial mass flow rate.

4.5. Effect of different power to mass flow rate ratios

In two previous subsections, the effects of initial power and initial mass flow rate on the transient behaviour were explained separately, while keeping the other parameter constant. When one of these parameters was changed, the hydrodynamic steady state of the system was changed by modifying the temperature rise along the core.

It was observed that lower power and lower mass flow rate had opposite effects on the peaks. At lower initial power, ***peak 1*** was present and ***peak 2*** was more pronounced. At lower initial mass flow rate, ***peak 1*** was not visible and ***peak 2*** was less pronounced.

In this subsection, the ULOF transient is analysed under conditions when the ratio of initial power to initial mass flow rate is constant, i.e. the steady-state core temperature remains unchanged. For the heat exchanger temperature $T_{HX} = 850$ K, and the coast-down time $CDT = 10$ s, two values of the power-to-mass-flow-rate ratio (further referred to as the ratio) P_0 / $MFR = 8000$ and 32000 W s/kg are selected. The initial mass flow rate is such to correspond to the initial power range $P_0 = 0.8$ - 3.2 MW (see Table 11).

In Fig. 12 and Fig. 14, the ULOF transient is shown for the ratio P_0 / $MFR = 8000$ W s/kg, and P_0 / $MFR = 32000$ W s/kg, respectively, and corresponding reactivity changes are shown in Fig. 13 and Fig. 15.

At lower ratio P_0 / MFR, ***peak 1*** is present in all cases. At lower initial mass flow rate and lower initial power, ***peak 1*** is more pronounced and ***valley 1*** is deeper than for higher values of these parameters. It indicates that the low-power effect of positive DNP reactivity insertion dominates the effect of the mass flow rate reduction. When the negative temperature feedback becomes more important, the mass flow rate effect becomes dominant, leading to a deeper ***valley 1*** for lower power and mass flow rate.

The positive temperature feedback then becomes more important and ***peak 2*** is significantly higher for lower mass flow rate and power, due to increased cooling and lower core heating. Additionally, the power oscillations are longer lasting (see Table 12).

In Fig. 14, ULOF transients for $T_{HX} = 850$ K, $CDT = 10$ s, P_0 / $MFR = 32000$ W/kg are shown, and corresponding reactivities for selected cases are shown in Fig. 15. Here, no ***peak 1*** is observed, and the difference in reactivity contributions is reflected in the initial slope of power decrease. For lower powers, the curve decreases more slowly compared to higher powers. For the smallest initial power ($P_0 = 0.8$ MW), the power drops to the deepest ***valley 1***, from which it increases to reach the highest ***peak 2*** among the considered curves. At higher power, the strong and rapid change in the reactivity due to the temperature increase dominates over the DNP reactivity insertion caused by the velocity decrease.

5. Summarized results

In this section, the effect of a change in all previously changed parameters on ***peak 1***, ***peak 2***, and ***valley 1*** is discussed. The relative amplitudes of the peaks and the valley are calculated and shown as a heat map. If the corresponding peak or valley was too small to be detected, the value is indicated in grey. Each figure consists of 12 subfigures corresponding to the three heat exchanger temperatures T_{HX} and the four initial powers P_0. In each subplot, the effect of variations in the mass flow rate (MFR) and the coast-down time (CDT) is shown.

In Fig. 16, the ***peak 1***-to-P_0 ratio is shown. For all powers and heat

Table 11
Parameters used to study the effect of P_0 / MFR.

P_0 [MW]	P_0 / MFR	T_{HX} [K]	CDT [s]
0.8, 1.6, 2.4, 3.2	8000, 32000	850	10

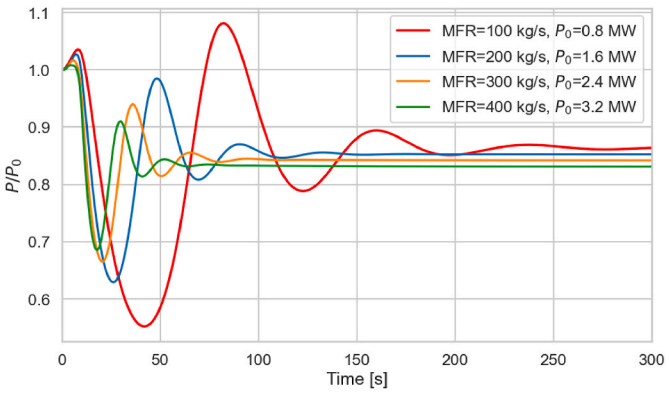

Fig. 12. Power change during the ULOF transient for different MFR and P_0 with $T_{HX} = 850$ K, $CDT = 10$ s, P_0 / $MFR = 8000$ W · s/kg ($\Delta T = 12.3$ K).

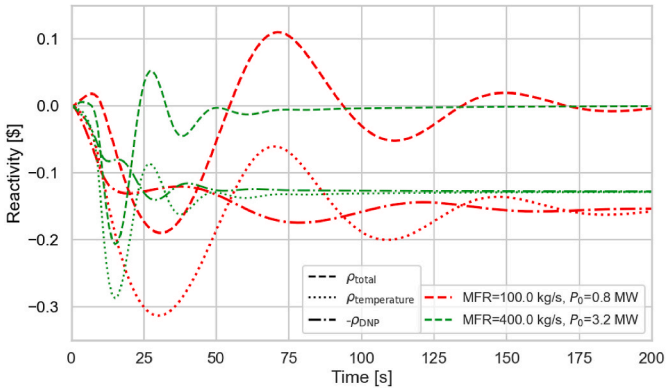

Fig. 13. Reactivity change during the ULOF transient for different MFR and P_0 with $T_{HX} = 850$ K, $CDT = 10$ s, P_0 / $MFR = 8000$ W · s/kg ($\Delta T = 12.3$ K).

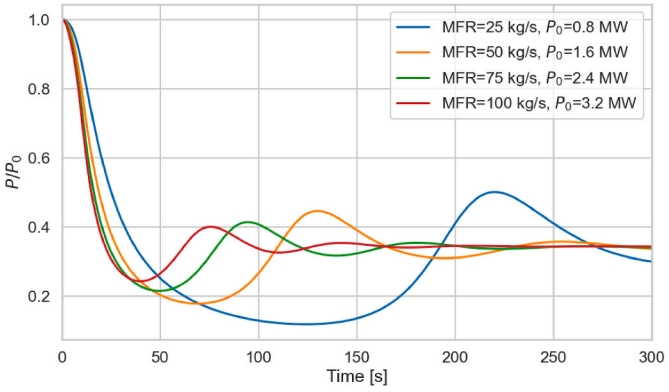

Fig. 14. Power change during the ULOF transient for different MFR and P_0 with $T_{HX} = 850$ K, $CDT = 10$ s, P_0 / $MFR = 32000$ W · s/kg ($\Delta T = 47.7$ K).

Table 12
Summary of MFR, P_0, and combined effects.

	peak 1	***valley 1***	***peak 2***
Low MFR	low	deep	low
Low P_0	high	shallow	high
Low P_0 and MFR	high	deep	high

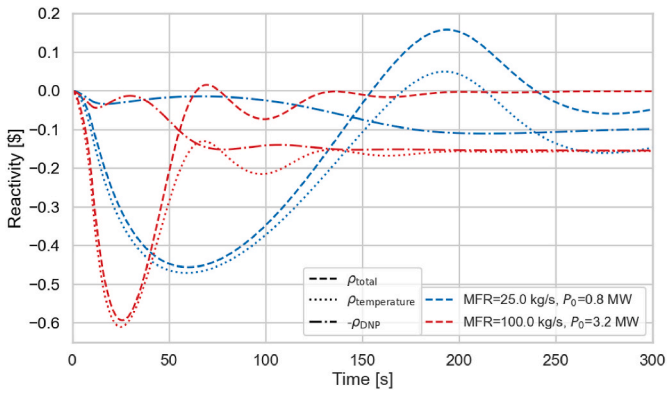

Fig. 15. Reactivity change during the ULOF transient for different *MFR* and P_0 with $T_{HX} = 850$ K, $CDT = 10$ s, P_0 / $MFR = 32000$ W · s/kg ($\Delta T = 47.7$ K).

exchanger temperatures, a larger *MFR* and a larger *CDT* result in an increase of the amplitude of ***peak 1***. For lower initial power and lower heat exchanger temperatures, ***peak 1*** is more pronounced.

In Fig. 17, the **valley *1***-to-P_0 ratio is shown. For all powers and heat exchanger temperatures, a larger *MFR* and a larger *CDT* results in a decrease of the amplitude of **valley *1***. For lower initial power and higher heat exchanger temperatures, **valley *1*** is more pronounced.

In Fig. 18, the ***peak 2***-to-P_0 ratio is shown. ***Peak 2*** is unique in the sense that it can be larger or smaller than the initial power P_0. For all powers and heat exchanger temperatures, a larger *MFR* and a smaller *CDT* result in an increase in the magnitude of ***peak 2***. For lower initial power and lower heat exchanger temperatures, ***peak 2*** is more pronounced.

5.1. *Special cases*

In Section 4, some illustrative transients were shown to better understand the general trends in power evolution during a ULOF event. However, not all transients exactly follow the pattern presented before. In this section, several non-standard cases are presented to demonstrate that the identification of peaks and valleys is not always straightforward and it will be explained why some transients reported in the literature may appear different [18,19].

It has already been shown that ***peak 1*** is not always present (Fig. 7,

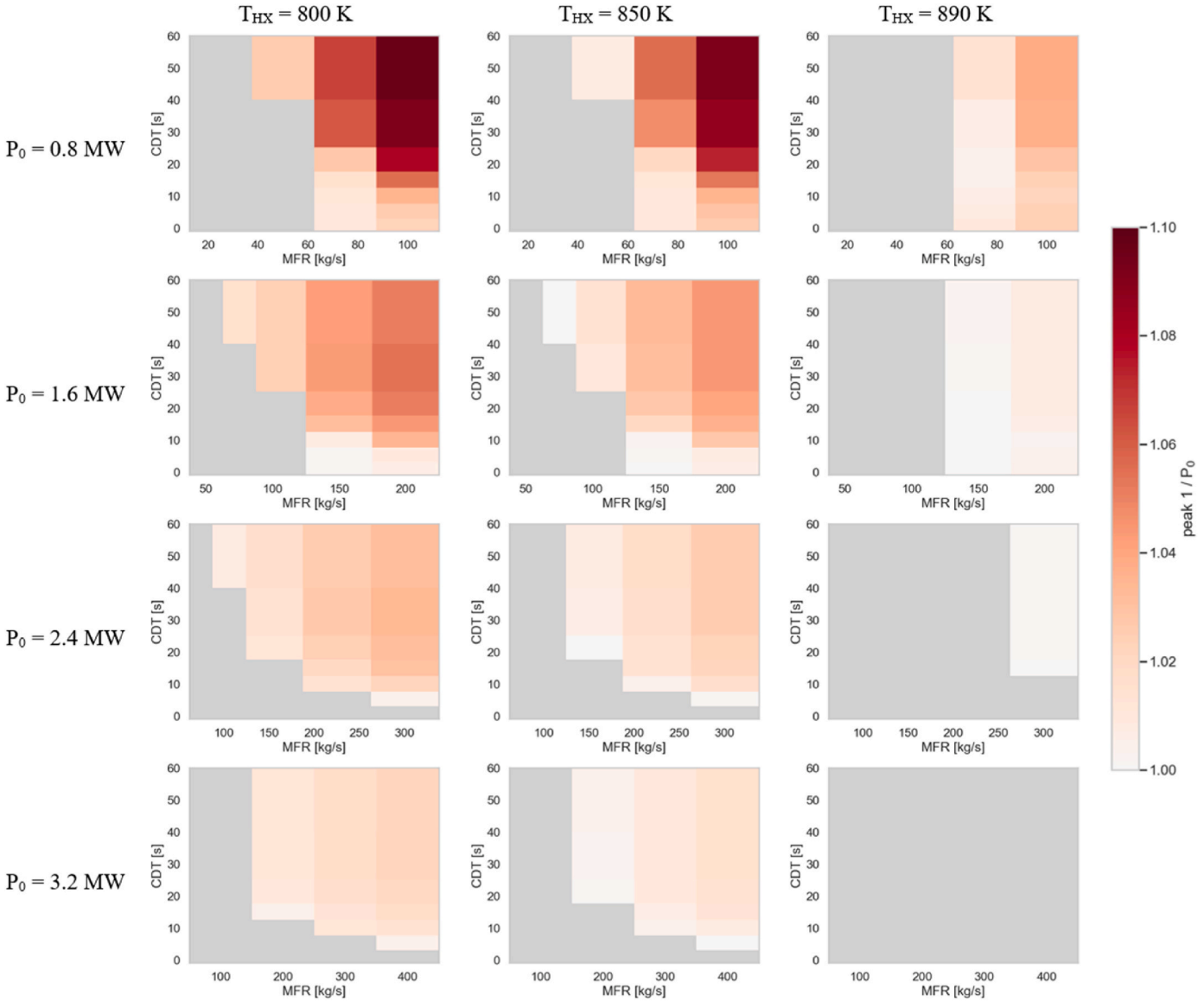

Fig. 16. Summarized results for ***peak 1*** magnitude/P_0.

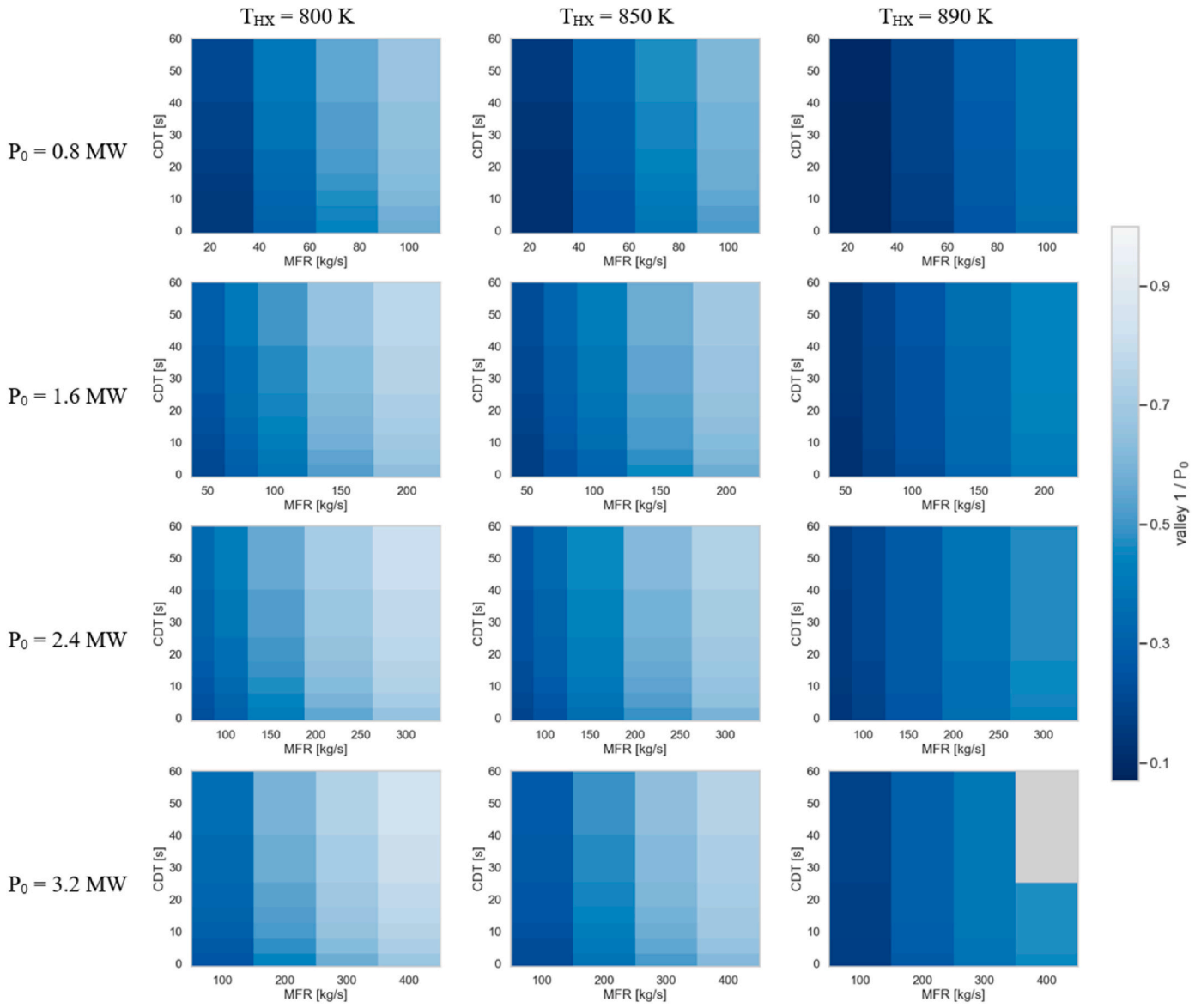

Fig. 17. Summarized results for ***valley 1***/P_0.

Fig. 10), particularly at higher power, where the power curve may immediately decrease after the transient is initiated. However, a short initial power drop should not be interpreted as a direct transition toward valley 1. In particular during the slow transients (characterised by large *CDT*s), the reactivity insertion due to the DNP retention can be delayed in time. As a result, a secondary increase in power may occur after an initial decrease, leading to a non-monotinic behaviour before ***peak 1***, as shown in Fig. 19.

Such a delayed increase of power due to the DNP retention might be also small enough not to be a local maximum. In such cases, for example for the initial mass flow rate $MFR = 50$ kg/s, initial power $P_0 = 1.6$ MW, $T_{HX} = 800$ K, $CDT = 50$ s (Fig. 20), no clear ***peak 1*** can be identified and only a small inflection corresponds to the DNP effect.

Another important observation is that in certain conditions ***peak 2*** can significantly diminish or disappear. In Fig. 16, ***peak 2*** was not detected for higher power, higher mass flow rate, higher heat exchanger temperature and large coast-down time. The reason is that the power curve during the ULOF transient becomes so smooth due to the very fast and strong evolution of the temperature feedback which strongly dominates the DNP feedback. This happens with higher mass flow rates and higher power, at higher heat exchanger temperature, as in Fig. 21. In this case, the location of the ***peak 2*** is rather a small inflection, with no local extrema, than a minimum of a ***valley 1*** and maximum of ***peak 2***.

It can be also noted that identification of ***valley 1*** is not as straightforward as it might seem from examples in Section 4. It does not always correspond to a global minimum and should be rather defined as the local minimum between the two peaks. In some cases, such as $MFR = 400$ kg/s, initial power $P_0 = 3.2$ MW, $T_{HX} = 890$ K and $CDT = 30$ s (Fig. 21), the power curve becomes so smooth that neither ***valley 1*** nor ***peak 2*** can be identified. This demonstrates that the peak/valley terminology may lose its meaning in certain operational regions.

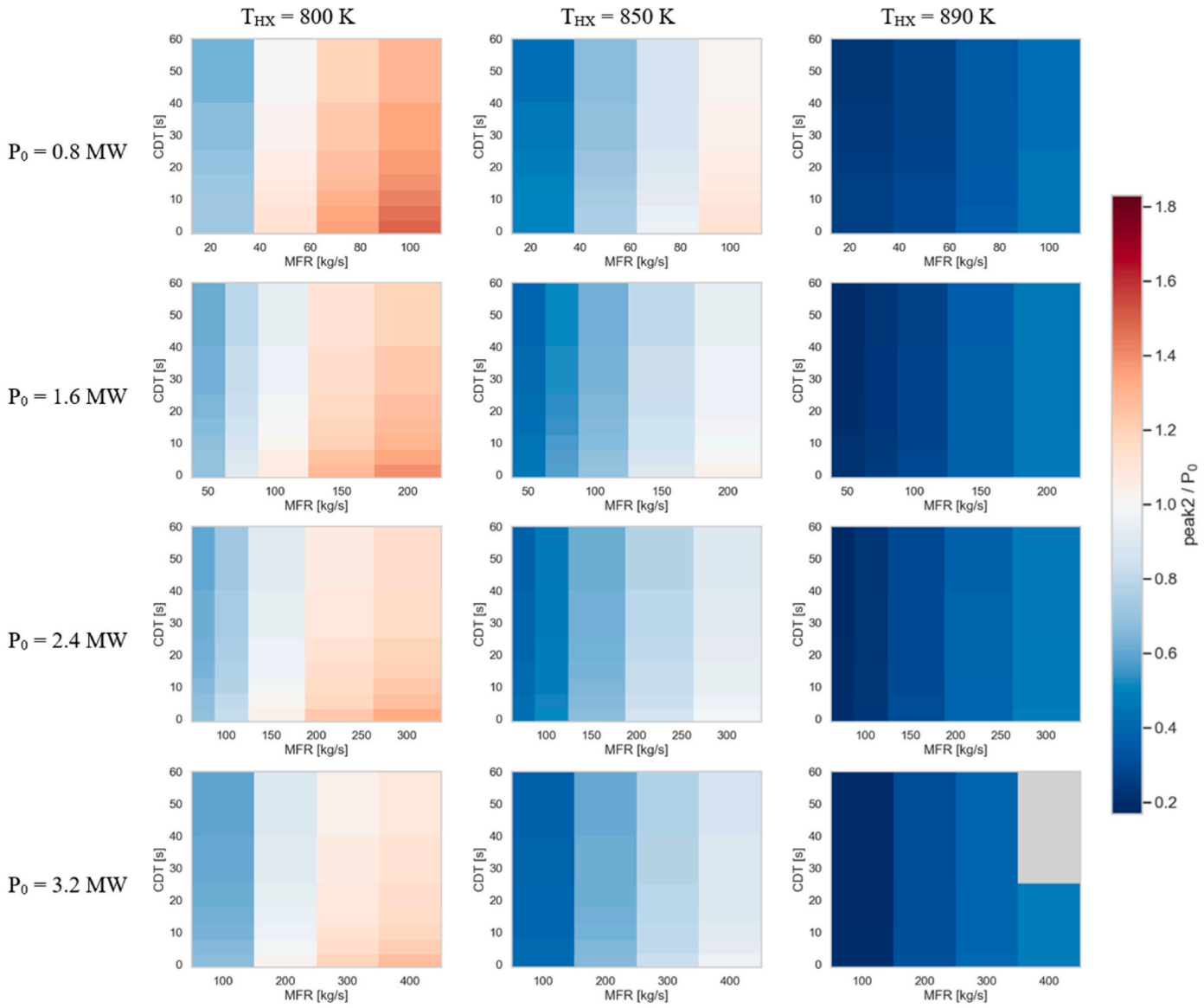

Fig. 18. Summarized results for ***peak 2***/P_0.

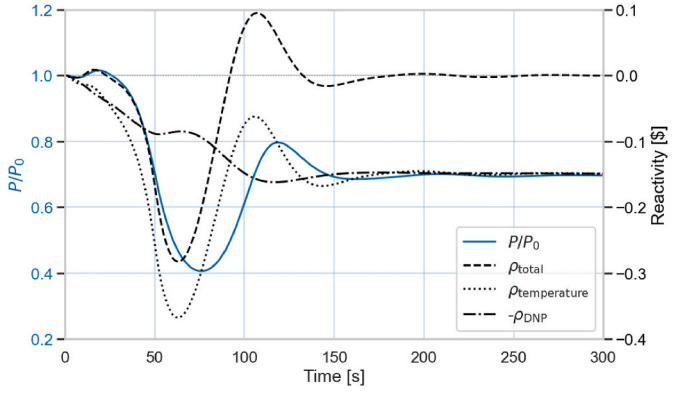

Fig. 19. Power and reactivity change during the ULOF transient with $MFR = 75$ kg/s, $P_0 = 1.6$ MW, $T_{HX} = 800$ K, $CDT = 50$ s.

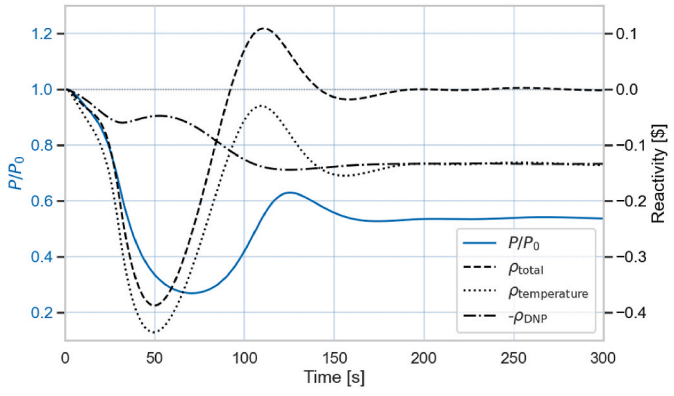

Fig. 20. Power and reactivity change during the ULOF transient with $MFR = 50$ kg/s, $P_0 = 1.6$ MW, $T_{HX} = 800$ K, $CDT = 30$ s.

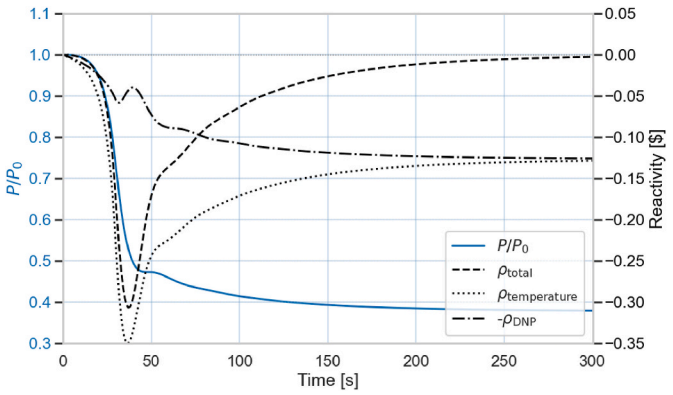

Fig. 21. Power and reactivity change during the ULOF transient with $MFR = 400$ kg/s, $P_0 = 3.2$ MW, $T_{HX} = 890$ K, $CDT = 30$ s.

6. Conclusion

In this paper, the dynamic response of a fast-spectrum molten chloride reactor to an unprotected loss-of-flow transient was studied, and the mechanisms underlying the characteristic double-peak behaviour were identified and explained. The results confirm that this behaviour arises from the interplay between delayed neutron precursor transport and temperature feedback - and demonstrate for the first time that it persists in a fast-spectrum chloride system, extending prior findings beyond thermal MSR designs. The occurrence and magnitude of the two peaks are, however, dependent on the reactor configuration and operating conditions.

The first power peak (***peak 1***) is caused by DNP retention in the core during flow reduction. Its magnitude increases with higher initial mass flow rate, lower initial power, longer coast-down time, and lower heat exchanger temperature. It is suppressed when the negative temperature feedback is sufficiently strong, i.e. at higher initial power levels.

The subsequent valley (***valley 1***) results from negative temperature feedback as the fuel heats up. It deepens with higher heat exchanger temperature, lower initial power, lower mass flow rate, and short coast-down time.

The second peak (***peak 2***) arises from the delayed return of colder fuel from the heat exchanger, inserting positive reactivity into the core. Notably, under certain operating conditions this peak can exceed the steady-state power level, which has direct implications for safety margin assessment. Its magnitude is amplified at lower heat exchanger temperatures, higher mass flow rates, lower initial power, and short coast-down times, and is damped by strong temperature feedback at higher power.

A proportional increase of both mass flow rate and initial power was shown to reduce the amplitude of both peaks and decrease the valley depth. Parametric maps of the extrema magnitudes across the studied operating space were presented, providing physical insight into parameter dependencies that can inform future safety analyses.

These results demonstrate that the ULOF response of an MSR is highly sensitive to steady-state operating parameters, including mass flow rate, power level, and heat exchanger temperature. Systematic characterisation of these dependencies is essential for defining safe operating envelopes and informing reactor control strategies. The findings are particularly relevant for startup conditions, where reduced power and thermal feedback may amplify the transient peaks described here.

The present study assumes plug flow and a single simplified reactor geometry; future work should examine the influence of turbulent flow profiles, multi-channel effects, and alternative chloride salt compositions on the observed behaviour. In particular, different heat exchanger designs or accident-induced changes in heat exchanger performance may substantially modify the delayed return of cooled fuel and consequently the second power peak. In addition, uncertainties in the thermophysical properties of chloride fuel salt may affect the ULOF response. A systematic uncertainty analysis would require physically consistent variations of the temperature-dependent salt properties within the equation-of-state formulation, rather than independent variations of individual properties. The propagation of salt-property uncertainties through the EOS and their influence on the transient response will therefore be addressed in future work. Extension of the parametric study to protected transients and different coast-down profiles would further support the development of validated safety analysis tools for fast MSR licensing.

CRediT authorship contribution statement

Barbara Kędzierska: Writing – review & editing, Writing – original draft, Visualization, Software, Methodology, Investigation, Formal analysis, Data curation, Conceptualization. **Philip Pfahl:** Writing – review & editing, Writing – original draft, Visualization, Methodology, Investigation, Formal analysis, Data curation, Conceptualization. **Andrei Rineiski:** Writing – review & editing, Supervision, Funding acquisition, Formal analysis.

Declaration of competing interests

The authors declare that they have no known competing financial interests or personal relationships that could have appeared to influence the work reported in this paper.

Acknowledgment

The authors would like to express their gratitude to the JAEA for the provision of SIMMER under a JAEA-KIT/CEA agreement on the exchange of information and collaboration to develop the code.

References

[1] J. Serp, et al., The molten salt reactor (MSR) in generation IV: overview and perspectives, Prog. Nucl. Energy 77 (Nov. 2014) 308–319, https://doi.org/10.1016/j.pnucene.2014.02.014.
[2] J. Krepel, U. Rohde, U. Grundmann, F.-P. Weiss, Dynamics of molten salt reactors, Nucl. Technol. 164 (1) (Oct. 2008) 34–44, https://doi.org/10.13182/NT08-A4006.
[3] A. Cammi, C. Fiorina, C. Guerrieri, L. Luzzi, Dimensional effects in the modelling of MSR dynamics: moving on from simplified schemes of analysis to a multi-physics modelling approach, Nucl. Eng. Des. 246 (May 2012) 12–26, https://doi.org/10.1016/j.nucengdes.2011.08.002.
[4] D. Wooten, J.J. Powers, A review of molten salt reactor kinetics models, Nucl. Sci. Eng. 191 (3) (Sep. 2018) 203–230, https://doi.org/10.1080/00295639.2018.1480182.
[5] P. Pfahl, et al., Multi-physics benchmark for a thermal molten salt reactor, Nucl. Eng. Des. 449 (Apr. 2026) 114790, https://doi.org/10.1016/j.nucengdes.2026.114790.
[6] W.F.G. van Rooijen, H. Mochizuki, Analysis of the EBR-II SHRT-45R unprotected loss of flow experiment with ERANOS and RELAP, Sci. Technol. Nuclear Installations 2015 (1) (2015) 832721, https://doi.org/10.1155/2015/832721.
[7] B.E. Prince, S.J. Ball, J.R. Engel, P.N. Haubenreich, T.W. Kerlin, Zero-Power Physics Experiments on the Molten-Salt Reactor Experiment', Oak Ridge National Lab. (ORNL), Tenn. (USA), Feb. 1968.
[8] P. Pfahl, M.K. Jaradat, M.E. Tano, R.O. Freile, S.A. Walker, J. Ortensi, Comparison of spatial dynamics and point kinetics approaches in multiphysics modeling of the molten salt reactor experiment, Front. Nucl. Eng. 4 (Aug. 2025), https://doi.org/10.3389/fnuen.2025.1617048.
[9] LOTUS Molten Chloride Reactor LMCR | vtb [Online]. Available: https://mooseframework.inl.gov/virtual_test_bed/msr/lotus/. (Accessed 10 January 2025).
[10] M. Aghili Nasr, A. Zolfaghari, R. Akbari, A. Cammi, S. Amirkhosravi, Neutronic and fuel cycle performance analysis of fluoride and chloride fuels in Molten Salt Fast Reactor (MSFR), Nucl. Eng. Des. 413 (Nov. 2023) 112506, https://doi.org/10.1016/j.nucengdes.2023.112506.
[11] H. Yamano, et al., SIMMER-III: a computer program for LMFR core disruptive accident analysis. O-arai Engineering Center, Japan Nuclear Cycle Development Institute, Aug. 2003. JNC TN9400 2003-071.
[12] S. Wang, A. Rineiski, W. Maschek, Molten salt related extensions of the SIMMER-III code and its application for a burner reactor, Nucl. Eng. Des. 236 (14) (Aug. 2006) 1580–1588, https://doi.org/10.1016/j.nucengdes.2006.04.022.
[13] B. Kędzierska, A. Rineiski, Y. Tobita, Modified algorithm for taking into account delayed neutron precursor movement in the improved quasi-static scheme of the

SIMMER-III code. Presented at the International Conference on Mathematics and Computational Methods Applied to Nuclear Science and Engineering (M&C 2025), Denver, CO, USA, Apr. 2025, https://doi.org/10.13182/MC25-47190.
[14] N. Ullah, et al., MCRE design description in support of external model development, TerraPower, MCRE-ENG-PRSNT-0029 (Dec. 2022).
[15] R.C. Diniz, F.S. de S. da Rosa, A. da C. Gonçalves, Calculation of delayed neutron precursors' transit time in the external loop during a flow velocity transient in a Molten Salt reactors, Ann. Nucl. Energy 165 (Jan. 2022) 108640, https://doi.org/10.1016/j.anucene.2021.108640.
[16] J.-B. Valentin, M. Fratoni, D. Siefman, L. Jantzen, M. Hursin, Uncertainty quantification of Cl-35 nuclear data on a Molten Chloride Fast Reactor, Ann. Nucl. Energy 222 (Nov. 2025) 111529, https://doi.org/10.1016/j.anucene.2025.111529.
[17] T. Cisneros, et al., Reactivity impact of updated 35Cl nuclear data on the molten chloride reactor experiment, Nucl. Sci. Eng. 0 (0) (Nov. 2024) 1–11, https://doi.org/10.1080/00295639.2024.2413787.
[18] Z. Guo, D. Zhang, Y. Xiao, W. Tian, G. Su, S. Qiu, Simulations of unprotected loss of heat sink and combination of events accidents for a molten salt reactor, Ann. Nucl. Energy 53 (Mar. 2013) 309–319, https://doi.org/10.1016/j.anucene.2012.09.009.
[19] R. Li, M. Cheng, Z. Dai, Improvement of the delayed neutron precursor transport model in RELAP5 for liquid-fueled molten salt reactor, Nucl. Eng. Des. 394 (Aug. 2022) 111817, https://doi.org/10.1016/j.nucengdes.2022.111817.